AIAA JOURNAL
Vol. 36, No. 4, April 1998

Supersonic Breakaway Separation Past an Adiabatic Wavy Wall

Alric P. Rothmayer*
Iowa State University, Ames, Iowa 50011

Triple-deck free interactions for breakaway separation are computed for flow past an adiabatic wavy wall. These solutions depend on a phase shift, which positions the breakaway separation relative to the wavy wall. It is found that the downstream shear layer slope of the breakaway separation is largely unaffected by the wavy wall.

Nomenclature

A = displacement function
F = wall geometry
h = height of wavy wall
k = gridpoint for periodicity condition
m = exponent of growing wavy wall
N = maximum Y gridpoint
P = pressure
P_0 = far downstream pressure asymptote and slope of breakaway shear layer
T = fictitious time
U = streamwise velocity
V = normal velocity
X = streamwise coordinate
Y = normal coordinate
β = pressure gradient
ΔT = fictitious temporal step
ΔX = streamwise grid spacing
κ = relaxation parameter
λ_X = streamwise wavelength of wavy wall
χ = streamwise phase shift of wavy wall

Subscripts

i = streamwise X gridpoint
j = vertical Y gridpoint

Superscript

g = guessed values

Central Triple-Deck Problem

THE triple-deck structure and the breakaway separation eigensolution are given in the studies of Neiland[1] and Stewartson and Williams.[2] The main assumptions of the triple-deck equations used in this study are that the Reynolds number is large, the Mach number is finite and supersonic, and the wavy wall is adiabatic, or approximately constant temperature. The Reynolds number scalings of the triple deck are shown in Fig. 1, where the Reynolds number $Re = Y_\infty V_\infty L/\mu_\infty$ is based on a characteristic velocity V_∞, density Y_∞, and viscosity μ_∞, typically taken to be freestream values. L is a characteristic length of the body in question. The triple deck involves an interaction between a slow moving viscous sublayer, or lower deck, and a predominantly inviscid outer deck, as shown in Fig. 1. The interaction occurs through a passive main deck, which is a linearized displacement of the oncoming boundary-layer flow. Because the flow velocities within the lower deck are close to zero, it can be described by a low Mach number approximation. The further assumption of an adiabatic, or almost constant temperature, wall, leads to incompressible flow in this layer, which is found to be governed by the incompressible boundary-layer equations

$$U_X + V_Y = 0 \tag{1}$$

and

$$UU_X + VU_Y = -\beta + U_{YY} \tag{2}$$

where $\beta = P_X(X)$ is the pressure gradient, X and Y are the scaled streamwise and normal coordinates within the lower deck (after a coordinate shearing transformation has been applied; see Fig. 1), and U and V are the scaled and shear transformed lower-deck velocity components in the X and Y directions, respectively. One boundary condition is matching with the main deck:

$$U \to Y + A(X) + F(X) \qquad \text{as} \qquad Y \to \infty \tag{3}$$

where Y is effectively the shear profile of the oncoming boundary layer, $A(X)$ is proportional to the displacement thickness of the viscous sublayer, and $F(X)$ is the wall shape. Two transformations have been applied to the preceding equations. One removes constant parameters in the equations, such as the upstream shear stress, the Mach number, and the Chapman viscosity constant. The other is a coordinate shearing transformation, which introduces $F(X)$ to Eq. (3). The reader may consult Ref. 3 for further details. The remaining boundary conditions are no-slip conditions applied at the surface of the wavy wall. In the body-fitted sheared coordinates these are

$$U(X, 0) = V(X, 0) = 0$$

The inviscid outer-deck flow is governed by a supersonic small-disturbance equation, whose solution gives Ackeret's law

$$P = -A_X \qquad \text{or} \qquad \beta = -A_{XX} \tag{4}$$

Numerical Methods for the Boundary-Layer Equations

The boundary-layer algorithms used here closely parallel those used by Veldman[4] and Davis and Werle[5] for the interacting boundary-layer equations. In all algorithms, one of the following is introduced for the pressure or pressure gradient:

$$\beta_Y = 0, \qquad P_Y = 0$$

These equations, together with the mass and momentum equations (1) and (2), are Newton linearized and parabolically differenced in a second-order accurate manner. In regions of flow reversal either a second-order upwind difference method or a FLARE approximation is used, i.e., neglect UU_X when $U < 0$. The resulting system of finite difference equations is inverted in the Y direction at each streamwise X station using a block tridiagonal algorithm. The boundary conditions at the wall are the two no-slip conditions, $U = V = 0$. At large Y, the boundary condition is Eq. (3).

If $A(X)$ and $F(X)$ in Eq. (3) are known functions of X, then the resulting finite difference equations can be iterated to convergence at each streamwise station, for attached flows, and the solution

Received Feb. 28, 1997; revision received Nov. 26, 1997; accepted for publication Dec. 3, 1997.

*Professor, Aerospace Engineering and Engineering Mechanics Department, 304 Town Engineering Building. Member AIAA.

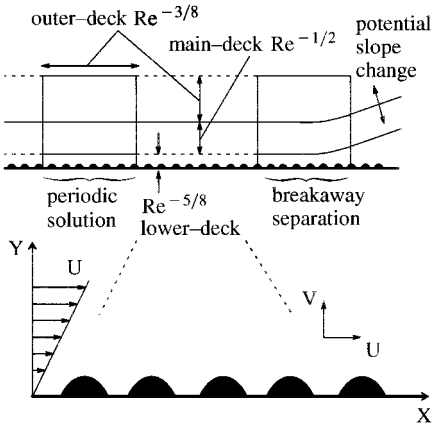

Fig. 1 Supersonic triple deck.

consists of a single parabolic pass in X. Introducing a $P(A)$ or $\beta(A)$ relation of form (4) does not allow a single-pass solution. Rather, Eq. (4) must be differenced to allow the solution at a particular X station to react to downstream effects. A multiple pass upstream to downstream solution, or global iteration, is then implemented with the Newton linearization and boundary value problem for $A(X)$ converged simultaneously.

The preceding algorithm is accelerated using two different methods, to be discussed subsequently. In all cases, the acceleration consists of a single downstream pass of the global iteration followed by the inversion of a single ordinary differential equation in X for $A(X)$.

Numerical Methods for Globally Iterated Supersonic Flows

In all cases, the finite difference form of the boundary condition (3), i.e.,

$$U_{iN} = Y_N + A_i + F_i$$

is rewritten in one of the following forms by using a $P(A)$ or $\beta(A)$ relation (4):

$$U_{i,N} + C_i P_{i,N} = R_i \tag{5a}$$

or

$$U_{i,N} + C_i \beta_{i,N} = R_i \tag{5b}$$

where N is the topmost gridpoint in the Y direction. The coupling is completely implicit in the sense of a Veldman[4] and Davis and Werle[5] algorithm because the entire effect of the local displacement function is removed and written in terms of variables within the boundary layer.

Pressure-Based Algorithm

The $P(A)$ relation (4) is forward differenced to allow the triple deck to react to downstream boundary conditions, in the form

$$P_{i,N} = -(A_X)_i = -\frac{-3A_i + 4A_{i+1} - A_{i+2}}{2\Delta X}$$

Solving for A_i and substituting into the U-matching condition (3) gives an equation of the form of Eq. (5a). This method converges very slowly, if at all. The convergence problem was circumvented by the alternating direction explicit (ADE) method of Davis.[6] The ADE method will be discussed in the Acceleration Schemes section.

Pressure-Gradient-Based Algorithm

The interaction law, $\beta(A)$, for the triple deck in pressure gradient form is given by the following central differenced expression:

$$\beta_{i,N} = -(A_{XX})_i = -\frac{A_{i-1} - 2A_i + A_{i+1}}{\Delta X^2}$$

Solving this equation for A_i and substituting into Eq. (3) gives the following form of the boundary condition (5b):

$$U_{i,N} - \frac{\Delta X^2}{2}\beta_{i,N} = Y_N + \frac{A_{i-1} + A_{i+1}}{2} + F_i$$

This method is reasonably stable, but also converges slowly (see Fig. 2).

Convergence Issues

The convergence of the triple-deck method for supersonic interactions is usually controlled by the amount of upstream influence present in the flow. That is, convergence is controlled by the relative importance of the downstream A_i. To illustrate this idea, consider the pressure gradient algorithm

$$\beta = P_X = -A_{XX} \tag{6}$$

A second-order accurate central difference of this $\beta(A)$ relation is

$$\beta_{i,N} = -(A_{XX})_i = -\frac{A_{i+1} - 2A_i + A_{i-1}}{\Delta X^2}$$

This equation gives a 2/1 ratio for the effect of A_{i+1} on the local solution, when compared to A_i, giving a weighting factor of 2.0. On the other hand, a fourth-order central difference of this same equation gives

$$\beta_{i,N} = -\frac{1}{12\Delta X^2}[-A_{i+2} + 16A_{i+1} - 30A_i + 16A_{i-1} - A_{i-2}]$$

The fourth-order central difference formula has a 30 to $16 + 1 = 17$ weighting of local to downstream influence, for a weighting factor of 1.7. Therefore, the second-order scheme has less downstream influence, i.e., a larger local weighting factor. The weighting factor of the second-order method is about 17–18% larger than that of the fourth-order scheme, and so it should converge approximately that much faster. This, in fact, happens, as shown in Fig. 2. The described methods were used in the fully second-order accurate quasisimultaneous scheme to solve the initial portion of the smooth surface free interaction using both FLARE and a second-order upwind difference, with $A = 0$ upstream and $A = -5$ downstream [on an interval $X = (0, 15)$, $Y = (0, 20)$ with 51 points in each direction]. In all cases exactly the same fully second-order accurate difference scheme was used with a modification only to the $P(A)$ or $\beta(A)$ relation and the pressure gradient term in the momentum equation. All schemes gave the same solution for wall shear (which has the last station near the minimum negative shear position, approximately $X = 11$ in Figs. 3 and 4). The error shown in Fig. 2 is a spatially averaged percent error of wall shear for the cases using FLARE. Figure 2 shows that there is about a 20% slow down from

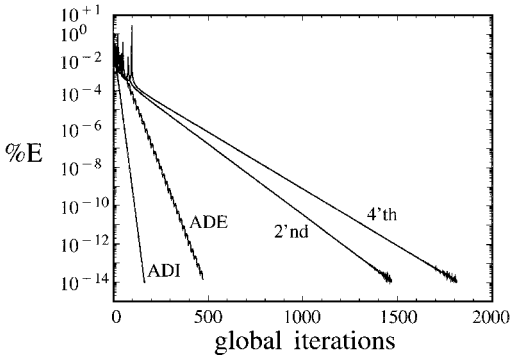

Fig. 2 Convergence comparisons of pressure-gradient-based second- and fourth-order line relaxations, and the ADI and Davis[6] ADE acceleration methods.

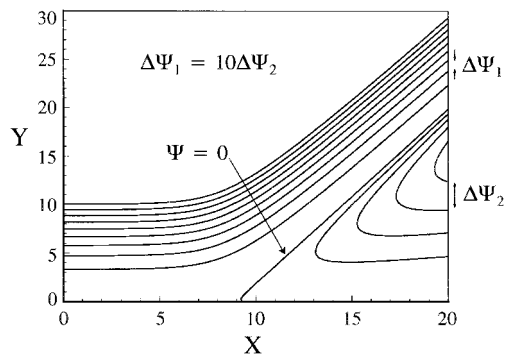

Fig. 3 Streamlines for breakaway separation past a smooth wall.

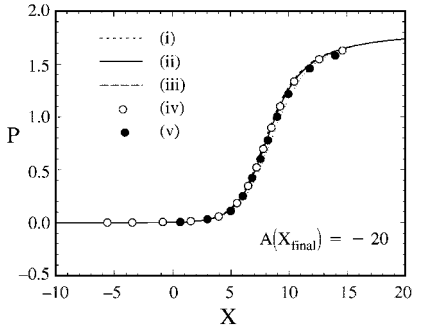

Fig. 4 Grids: i) 50, 50; ii) 100, 100; iii) 150, 150; iv) $A(X_{\text{final}}) = -12$, upwind, converged two orders of magnitude more, are compared with v) Stewartson and Williams[2] results.

the second- to the fourth-order scheme, as expected, i.e., 1469 iterations to convergence for the second-order scheme vs 1811 for the fourth-order scheme. Also shown are the ADE and alternating direction implicit (ADI) schemes (to be discussed later), which both outperform the straightforward line relaxations. The ADE and ADI methods shown here both use optimal time steps (0.1 for the ADE and 0.8 for the ADI). The convergence rates of the ADI and ADE methods do depend sensitively on time steps. Part of the faster convergence for the ADI method is because it is stable for larger time steps.

Acceleration Schemes

Pressure-Based ADE Acceleration

The ADE method of Davis[6] introduces a fictitious time derivative into the interaction law, which tends to zero as the solution converges. The following form of the interaction law (4) is used, with the sign of the unsteady term chosen to give upstream propagating waves for prescribed pressure:

$$P = A_T - A_X \tag{7}$$

The ADE method is a two-pass procedure. First, the pressure interaction law is coupled to the U-matching condition. The pressure-displacement interaction law is differenced in a manner suitable for upstream propagating waves, i.e.,

$$P_{i,N} = \frac{A_i - A_i^g}{\Delta T} - \frac{-3A_i^g + 4A_{i+1}^g - A_{i+2}^g}{2\Delta X}$$

$$= \frac{A_i - A_i^g}{\Delta T} - A_X^g$$

except at the last point, where a first-order difference is used. The guessed value is fixed during a global iteration sweep. Note that only the pseudotime derivative is directly coupled to the boundary layer in the downstream pass. Isolating the local displacement A_i and combining the result with the U-matching condition (3) gives a boundary condition of the form of Eq. (5a):

$$U_{i,N} - \Delta T P_{i,N} = Y_N + A_i^g + \Delta T A_X^g + F_i$$

The second step of the ADE method consists of prescribing the pressure and solving the wave equation (7) for the displacement function $A(X)$. In finite difference form, this equation is solved from $i = M$ to $i = 1$ in the form

$$P_{i,N}^g = \frac{A_i - A_i^g}{\Delta T} - \frac{-3A_i + 4A_{i+1}^g - A_{i+2}^g}{2\Delta X}$$

The convergence acceleration of the ADE method is shown in Fig. 2.

Pressure-Gradient-Based ADI Acceleration

The ADI method proposed here is similar to the ADE method of Davis.[6] A fictitious temporal term is introduced into Eq. (6) in the form

$$\beta = A_T - A_{XX} = \frac{A_i - A_i^g}{\Delta T} - \frac{A_{i-1}^g - 2A_i + A_{i+1}^g}{\Delta X^2}$$

Solving for A_i and substituting into Eq. (3) gives the boundary condition in the form of Eq. (5b):

$$U_{i,N} - \left(\frac{1}{\Delta T} + \frac{2}{\Delta X^2}\right)^{-1} \beta_{i,j} = Y_N + F_i$$

$$+ \left(\frac{1}{\Delta T} + \frac{2}{\Delta X^2}\right)^{-1} \left[\frac{A_{i-1}^g + A_{i+1}^g}{\Delta X^2} + \frac{1}{\Delta T} A_i^g\right]$$

This equation is used as the boundary condition on the forward pass. After each forward pass, an ADI acceleration step is computed by inverting the following scalar tridiagonal equation:

$$-(1/\Delta X^2)A_{i-1} + [(1/\Delta T) + (2/\Delta X^2)]A_i - (1/\Delta X^2)A_{i+1}$$

$$= \beta_{i,j} + (1/\Delta T)A_i^g \tag{8}$$

This method has several advantages over the method of Davis.[6] First, the method operates on the pressure-gradient-based viscous-inviscid interaction problem, which is inherently more stable than the pressure-based method. Second, the boundary value inversion of Eq. (8) for $A(X)$ propagates information very quickly through the grid.

As noted in Fig. 2, this method is by far the fastest of all of the methods tested in this study and was the key to obtaining the highly separated breakaway solutions past the wavy wall. This method is particularly appropriate for the problem of local breakaway separation, because the downstream boundary condition is specified on $A(X)$. This boundary condition may take on almost any value and still be consistent with the free interaction, whereas a method that uses a downstream pressure differencing requires fixing the downstream pressure, and this may be difficult to pin down accurately.

Comparisons with Ref. 2

The free interaction for the supersonic triple-deck was first computed by Stewartson and Williams.[2] One viable approach for computing the free interaction for smooth walls is to use a forward marching method with a backward differenced $P(A)$ relation (4). This approach will not work for the roughness problem. The reason is that there are two types of free interactions: a compressive one computed by Stewartson and Williams,[2] which has rising pressure and leads to breakaway separation, and an expansive one computed by Brown et al.[7] (see also Ref. 8), which has falling pressure and rising displacement and leads to an acceleration of the flow terminating in a finite position singularity. The type of free interaction encountered depends on the upstream pressure perturbation. Positive pressure perturbations give rise to the compressive free interaction, and negative pressure perturbations give rise to the expansive one. Free interactions past roughness have both positive and negative pressure perturbations over the initial upstream roughness. This means that both free interactions are triggered, and it is likely that only the fastest growing one, namely, the expansive, will be encountered in numerical computations. In fact, this was found to be the case. All purely forward marching computations gave the expansive free interaction. This observation is the primary motivation for solving the free interaction using a global iteration method.

The streamline pattern for the globally iterated compressive free interaction and breakaway separation past a smooth wall is shown in Fig. 3. The linearly growing separation region is clearly seen.

Grid Study

Results for pressure are shown in Fig. 4. Also shown is a grid study on (50, 50), (100, 100) and (150, 150) grids. Grid independence is reached by the (100, 100) grid. Comparisons of these results with the results of Stewartson and Williams[2] are shown in Fig. 4.

Sensitivity to Downstream $A(X)$ and FLARE Approximation

On the downstream side of separation, the displacement function is continuously dropping, i.e., becoming large and negative. This means that any large negative value may be set for the downstream $A(X)$ boundary condition. Different downstream values of $A(X)$ simply give an origin shift in the solution. This result is shown in Fig. 4. The grid size study discussed earlier was conducted with

a FLARE approximation and a downstream boundary condition of $A = -20$ at the last gridpoint. Also shown in Fig. 4 is an upwind difference solution with a downstream boundary condition of $A = -12$ (note that the last two points were FLAREd, and the upwind method would not converge for sufficiently large separations).

Furthermore, a convergence criterion study was included in this case, with the convergence criterion lowered by two orders of magnitude. The results of this computation are shifted in X so that the separation point coincides with the (100, 100) case. As seen in Fig. 4, the results are essentially the same as the (100, 100) grid solution with $A = -20$ and a FLARE approximation.

Breakaway Separation Past a Wavy Wall

Computational Issues

Now consider the breakaway separation past the following uniform wavy wall:

$$F(X) = h \sin(2\pi/\lambda_X)(X - \chi)$$

The globally iterated ADI method based on pressure gradient was used to compute this flow. The following grid was assumed, where the downstream boundary is placed at P periods of the sine:

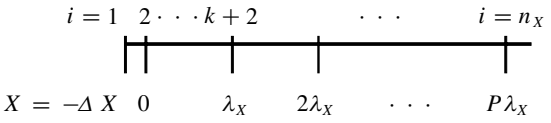

In the code, the number of gridpoints in the period λ_X is specified, i.e., k, as well as the total number of periods in the grid. The periodicity condition for the upstream flow is taken to be

$$U_{2,j} = U_{k+2,j}, \qquad U_{1,j} = U_{k+1,j} \tag{9}$$

$$V_{2,j} = V_{k+2,j}, \qquad V_{1,j} = V_{k+1,j} \tag{10}$$

and

$$A_2 = A_{k+2}, \qquad A_1 = A_{k+1} \tag{11}$$

These conditions were either enforced within the iteration cycle or between successive cases (to be discussed). The computations generally required cycling first through a series of hump heights starting from zero height and progressing to the final height, all with small downstream A_i. This solution was then used as an initial guess to cycle through a series of prescribed downstream A_i. The periodicity condition was fully converged within the first cycle, i.e., increasing height with downstream A fixed and small, although severe underrelaxation of the velocity conditions (9) was required, in the form

$$U_{2,j} = (1 - \kappa)U_{2,j} + \kappa U_{k+2,j}$$

No underrelaxation was used during the $A(X)$ cycle. It was found that the upstream periodicity condition could not be fully converged when the downstream $A(X)$ was large (or when it changed significantly from one case to the next). The difficulty was only encountered late in the iteration when the error was low. It is likely that a large and negative downstream $A(X)$ requires the first solution station to be placed far upstream of the breakaway separation to obtain an extremely accurate satisfaction of the periodicity condition. Unfortunately, that was not feasible for this problem (note that simply stretching the grid in X will not work here, as the grid must be uniformly extended on the upstream side to correctly capture the upstream periodic solution). Therefore, after the hump reached its final height, which more or less sets the upstream solution, the periodicity conditions (9–11) were fixed within each case but were updated from case to case, i.e., Eqs. (9–11) from a converged case were applied to the $i = 1, 2$ gridpoints and fixed for the subsequent case. Typically, anywhere from 5 to 200 cases were used for either the hump height increases or the variations of the downstream $A(X)$. Therefore, the upstream solutions are close to periodic, and the following results show that they are periodic to at least graphical accuracy.

Results

Figure 5 shows a grid convergence study for a typical wall shear solution for the wavy wall. The upstream periodic attached solution and the downstream breakaway separation shear stress are both clearly seen in Fig. 5.

Solutions with Phase Shift

Figures 6 and 7 show a series of solutions with the downstream value of A fixed at -15 and the hump center χ shifted from 0 to λ_X. As χ changes, the flow separates from different points along the wavy wall. In general, each of these solutions will be different (Figs. 7a–7e). Figures 7a–7e show the breakaway separation streamlines embedded within the otherwise periodic flow over the wall. Figure 8 shows the vorticity distribution. The upstream lobes of vorticity are the sublayer solution for the wavy wall. The vorticity concentration about the breakaway shear layer is also evident. Remember that the triple deck is a small-scale region embedded in a larger problem. The separation point may move on the longer scale and so the phase shift parameter can vary rapidly as the separation point moves a finite distance along a body surface. This means, effectively, that the phase shift is a stochastic variable. The separation should be viewed as an average separation with a random component generated by the phase shift. We can split the flow variables into the following components:

$$U(X, Y, \chi) = \bar{U}(X, Y) + U'(X, Y, \chi)$$

with similar expressions for the other variables. The average is defined to be an average over the phase shift

$$\bar{U} = \langle U(X, Y, \chi) \rangle = \frac{1}{\lambda_X} \int_0^{\lambda_X} U(X, Y, \chi)\, d\chi \tag{12}$$

We may then construct the average equation in the standard manner. This gives the following triple-deck problem: the conservation of mass equation (1), the no-slip boundary conditions, and the $P(A)$

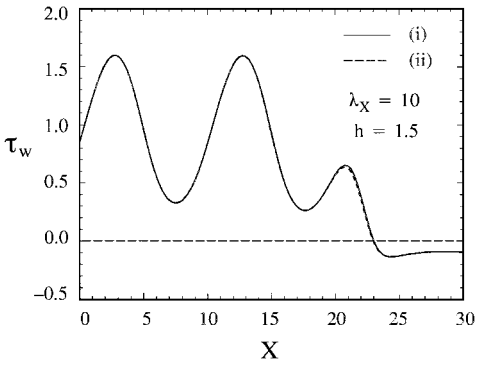

Fig. 5 Grid study for wall shear stress: i) (122, 101) grid, and ii) (182, 151) grid.

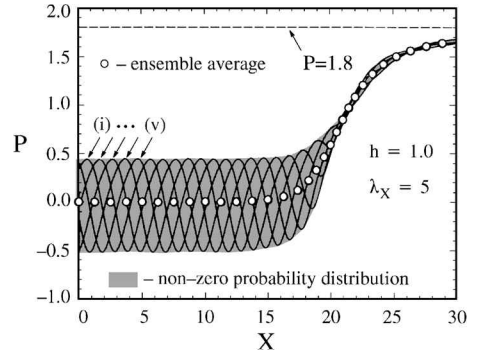

Fig. 6 Effect of phase shift on pressure: ϕ = i) 1.0, ii) 2.0, iii) 3.0, iv) 4.0, and v) 5.0, 0.0.

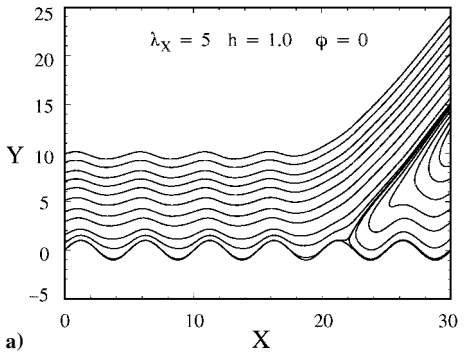

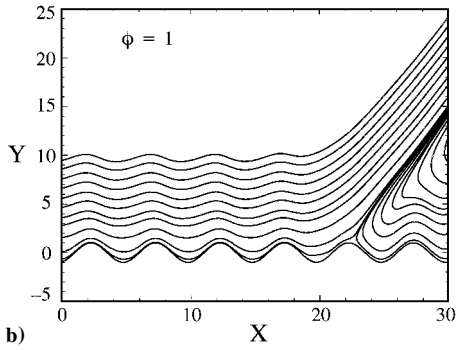

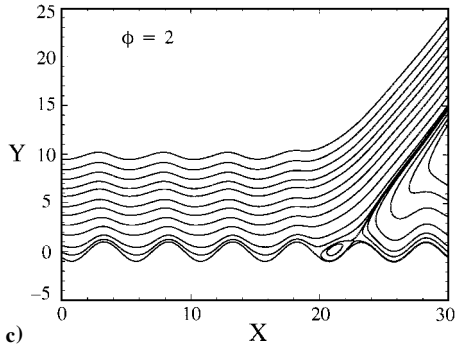

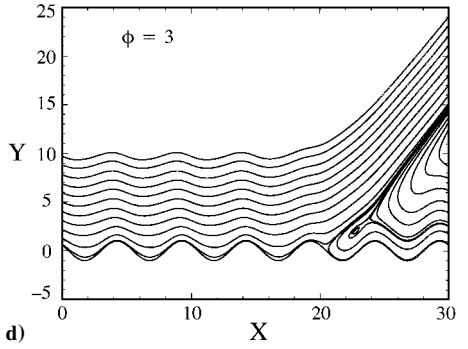

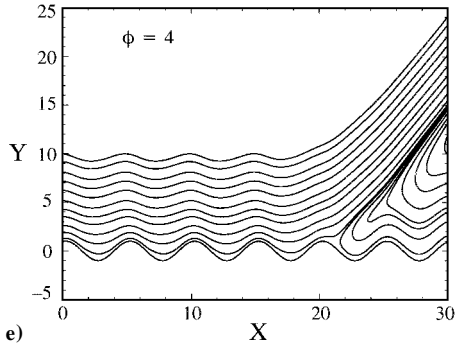

Fig. 7 Streamlines for the phase-shifted solutions of Fig. 6.

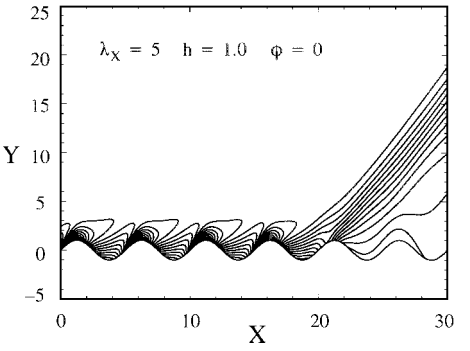

Fig. 8 Typical vorticity contours for the phase-shifted solutions of Fig. 6.

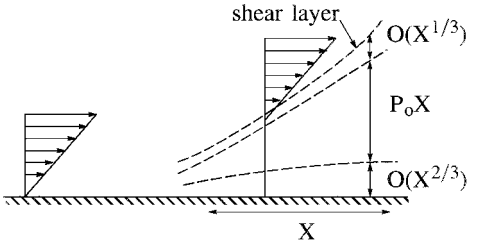

Fig. 9 Downstream asymptote of breakaway separation.

relation (4) retain the same form in the averaged variables. The momentum equation (2) becomes

$$\bar{U}\bar{U}_X + \bar{V}\bar{U}_Y + \langle U'^2\rangle_X + \langle U'V'\rangle_Y = -\bar{P}_X(X) + \bar{U}_{YY}$$

The U-matching condition (3) becomes

$$\bar{U} \to Y + \bar{A} + \bar{F}(X) \qquad \text{as} \qquad Y \to \infty$$

where, for this particular problem,

$$\bar{F}(X) = \frac{h}{\lambda_X}\int_0^{\lambda_X} \sin\frac{2\pi}{\lambda_X}(X-\chi)\,\mathrm{d}\chi = 0$$

This means that the average separation is a flow past a flat surface with the Reynolds stresses providing the forcing that accounts for the wavy wall.

The averaged solution for the pressure is also shown in Fig. 6 and is computed from a trapezoidal rule integration applied to Eq. (12), i.e.,

$$\bar{P}(X) = \frac{\Delta\chi}{\lambda_X}\left[\frac{P(X,\chi_1)+P(X,\chi_Q)}{2} + \sum_{k=2}^{Q-1} P(X,\chi_k)\right]$$

In Fig. 6, the number of integration points Q was chosen to be five, i.e., the five cases shown in Figs. 6 and 7, and so the average is not particularly accurate. However, it is likely that this figure is representative of a more accurate average. Also shown are the approximate bounds on the values the pressure can take, i.e., the region in which the probability density is nonzero. The hump has a wide range of allowable pressures in the upstream flow. As the flow breaks away from the body the allowable pressures rapidly collapse toward the average, suggesting that the downstream flow is not terribly sensitive to changes in surface geometry. In addition, the $P = 1.8$ downstream limit of Stewartson and Williams[2] is shown in Fig. 6, and the present solutions do not significantly deviate from that value.

Role of Downstream Pressure

The results of Stewartson and Williams[2] show that the downstream pressure asymptotes to a constant value of around $P = P_0 = 1.8$ in the smooth wall case. This pressure asymptote sets the breakaway shear layer slope via Eq. (4), i.e., the shear layer height is $S(X) = -A(X)$ and is given in the limit by

$$S(X) \to P_0 X \qquad \text{as} \qquad X \to \infty$$

The structure of the downstream limit solution is shown in Fig. 9, and details may be found in Ref. 2. The downstream shear layer slope

plays an important role in a larger scale separation, as it sets the angle of the separation bubble at the separation point. Any change in the downstream slope of the triple-deck shear layer induced by surface roughness, as manifested by a change in the downstream pressure asymptote, would be expected to affect the larger scale separation. Unfortunately, such a change is not evident in any of the solutions presented so far. This is an unusual result, in and of itself, because Stewartson and Williams[2] claim that the pressure asymptote cannot be fixed from a downstream limit solution but must be determined by nonlinear processes within the full triple-deck separation. The viscous triple-deck solution passing through separation is being significantly modified by the wall geometry in all computations presented in this study, but the downstream pressure is largely unaffected.

Higher Amplitude Solutions

The amplitude of the wavy wall was increased in an attempt to affect the downstream pressure asymptote and, thereby, the breakaway shear layer slope. A typical stream function solution for a wavy wall with moderate initial separation is shown in Fig. 10. An expanded view of a similar solution is shown in Fig. 11. Even though the initial breakaway slope is lowered near separation, the slope farther downstream returns to the smooth value (as shown in Fig. 11). A case with deep initial separation on the wavy wall is shown in Fig. 12, with an expanded view of a similar case shown

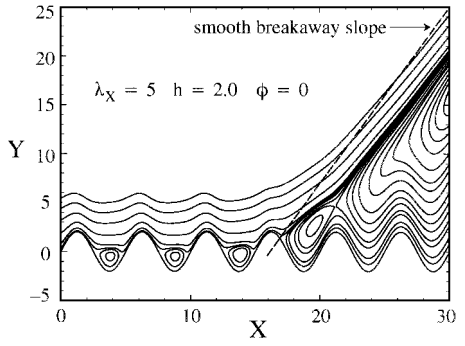

Fig. 10 Local view of breakaway separation past a wavy wall with moderate initial separation. Also shown is the downstream breakaway slope past a smooth wall (from Fig. 3).

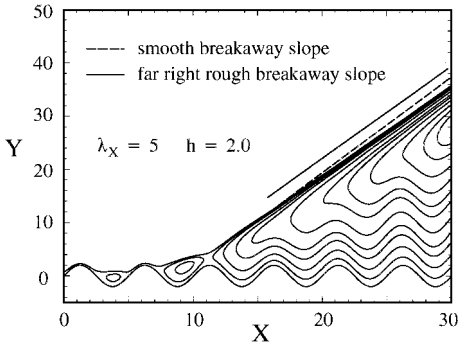

Fig. 11 Expanded view of the Fig. 10 wall with the computations carried farther downstream and comparison of the smooth and rough downstream shear layer slopes.

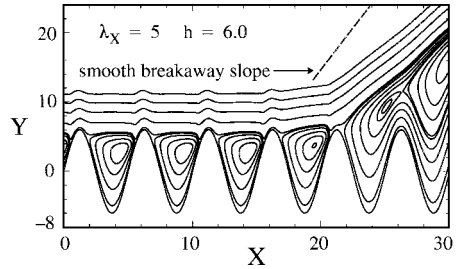

Fig. 12 Local view of breakaway separation past a wavy wall with deep initial separation. Also shown is the downstream breakaway slope past a smooth wall (from Fig. 3).

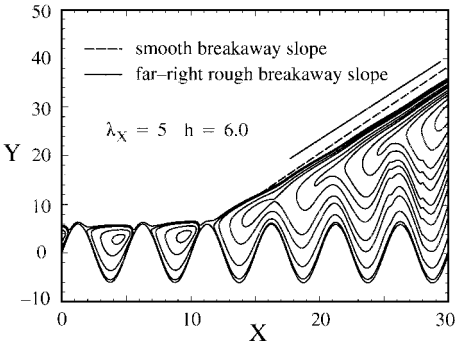

Fig. 13 Expanded view of the Fig. 12 wall with the computations carried farther downstream and comparison of the smooth and rough downstream shear layer slopes.

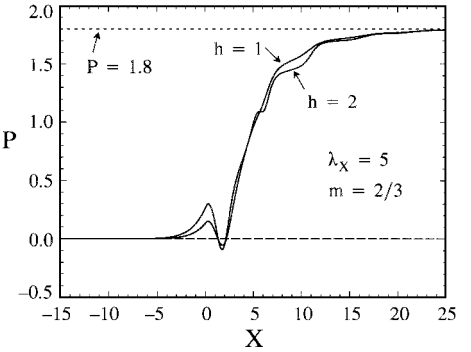

Fig. 14 Pressure for entry into a region where roughness height increases in proportion to $X^{2/3}$ [Eq. (13)].

in Fig. 13. Again, there is a decrease in slope near the separation point, but the smooth slope is recovered farther downstream. The pressures upstream of the breakaway separation vary significantly, but downstream of breakaway separation the pressures collapse to values close to the smooth wall case and show little dependence on the phase shift (results not shown).

Breakaway Separation Entering into a Roughness Patch

Clearly, if the supersonic breakaway separation lies just upstream of a roughness region, which is growing at a faster rate than the smooth breakaway shear layer, then that roughness must impact the downstream form of the separation. The goal here is to identify downstream roughness forms that could affect the separation, and that will be accomplished by examining the breakaway separation solution that is entering a region of nonuniform roughness. The breakaway separation is known to asymptote to the structure shown in Fig. 9. If the roughness grows fast enough downstream of the initial separation, then it should eventually impact the solution for the downstream asymptote. There are two cases that stand out. The first is when the roughness grows faster than the downstream reversed boundary layer, i.e., $X^{2/3}$. The second is when the roughness grows faster than the downstream reversed flow region, i.e., X.

The two standout cases will be examined using a roughness, which will be taken to be $F(X) = 0$ when $X < 0$ and

$$F(X) = h(X/\lambda_X)^m \sin[(2\pi/\lambda_X)X] \tag{13}$$

when $X > 0$. The function $F(X)$ is well behaved at $X = 0$. Solutions where the roughness height grows at a rate comparable to the reversed boundary-layer height are shown in Fig. 14. Nothing very interesting is seen here. In particular, there is no evidence of a change in the downstream pressure asymptote. Solutions where the roughness height grows in proportion to the height of the separated region are shown in Fig. 15. Here, a small but persistent change in the downstream pressure was observed, and the downstream pressure is increasing with increasing wall height. This means that the breakaway separation slope is becoming steeper, as might be expected due to the downstream flow blockage.

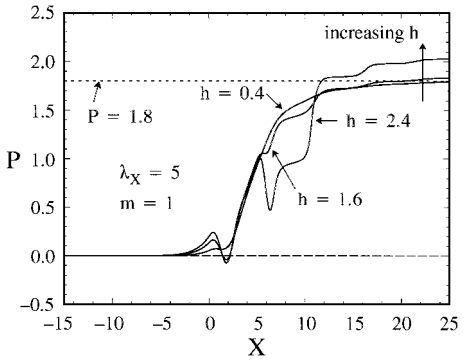

Fig. 15 Pressure for entry into a region where roughness height increases linearly with *X*.

Conclusion

Supersonic breakaway separation has been computed for flow past a wavy wall and other geometries simulating surface roughness. It was found that the free interaction of Neiland[1] and Stewartson and Williams[2] could be significantly modified by wall geometry in regions close to the initial separation. It was also found that the downstream asymptote remained largely unchanged.

Acknowledgments

This effort was sponsored by the U.S. Air Force Office of Scientific Research, Air Force Materials Command, under Grant F49620-95-1-0275. The author thanks J. Miller and J. Tsao for useful discussion pertaining to this work.

References

[1]Neiland, V. Y., "Theory of Laminar Boundary Layer Separation in Supersonic Flow," *Izvestiya Akademii Nauk SSSR, Mekhanica Zhidkosti i Gaza (Bulletin of the Academy of Sciences of the USSR, Mechanics of Liquids and Gases)*; translated in *Fluid Dynamics*, Vol. 4, No. 4, 1969, pp. 33–35.

[2]Stewartson, K., and Williams, P. G., "Self-Induced Separation I, II," *Proceedings of the Royal Society of London*, Vol. A312, 1969, pp. 181–206; also *Mathematika*, Vol. 20, 1973, pp. 98–108.

[3]Stewartson, K., "Multi-Structured Boundary Layers on Flat Plates and Related Bodies," *Advances in Applied Mechanics*, Vol. 14, 1974, pp. 145–239.

[4]Veldman, A. E. P., "A New Quasi-Simultaneous Method to Calculate Interacting Boundary Layers," *AIAA Journal*, Vol. 19, No. 1, 1981, pp. 79–85.

[5]Davis, R. T., and Werle, M. J., "Progress on Interacting Boundary Layer Computations at High Reynolds Numbers," *Numerical and Physical Aspects of Aerodynamic Flows*, Vol. 1, Springer–Verlag, New York, 1982, pp. 187–210.

[6]Davis, R. T., "A Procedure for Solving the Compressible Boundary-Layer Equations for Subsonic and Supersonic Flows," AIAA Paper 84-1614, June 1984.

[7]Brown, S. N., Stewartson, K., and Williams, P. G., "On Expansive Free-Interactions in Boundary Layers," *Proceedings of the Royal Society of Edinburgh*, Vol. 74A, No. 21, 1974, pp. 271–283.

[8]Neiland, Y. V., "Asymptotic Theory for Calculating Heat Flux Near the Corner of a Body," *Izvestiya Akademii Nauk SSSR, Mekhanica Zhidkosti i Gaza (Bulletin of the Academy of Sciences of the USSR, Mechanics of Liquids and Gases)*; translated in *Fluid Dynamics*, Vol. 4, No. 5, 1969, pp. 53–60.

W. Oberkampf
Associate Editor